Available online at www.sciencedirect.com
ScienceDirect
Surface Science 601 (2007) 3082–3098
SURFACE SCIENCE
www.elsevier.com/locate/susc

Adsorption of V on a hematite (0001) surface and its oxidation: Submonolayer coverage

Jianjian Jin [a], Xiaoyan Ma [b,c], C.-Y. Kim [d], D.E. Ellis [a,b,c,*], M.J. Bedzyk [c,d]

[a] Department of Physics and Astronomy, Northwestern University, Evanston, IL 60208, United States
[b] Department of Chemistry, Northwestern University, United States
[c] Institute of Environmental Catalysis, Northwestern University, United States
[d] Department of Materials Science and Engineering, Northwestern University, United States

Received 26 February 2007; accepted for publication 11 May 2007
Available online 24 May 2007

Abstract

The adsorption of submonolayer V on an idealized model hematite (0001) surface and subsequent oxidation under atomic O adsorption are studied by density functional theory. The preferred adsorption sites, adsorption energy and configuration changes due to V and O adsorption are investigated. It is found that in most cases V forms threefold bonds with surface O atoms, inducing a large geometry change at the hematite surface and near surface region and a bond stretch between surface Fe and O. The adsorption energy is mainly decided by interplay between adsorbed metal-surface oxygen bonding and adsorbed metal – subsurface metal interaction. The relative energy of subsequent O adsorption and geometry depends on the reformed V/hematite structure. Electronic properties such as projected densities of states and chemical state change upon V adsorption are studied through both periodic slab and embedded cluster localized orbital calculations; both strong vanadium–oxygen and vanadium–iron interactions are found. While V generally donates electrons to a hematite surface, causing nearby Fe to be partially reduced, the Fe and V oxidization state depends very much on the coverage and detailed adsorption configuration. When the V/hematite system is exposed to atomic O, V is further oxidized and surface/near surface Fe is re-oxidized. Our theoretical results are compared with X-ray surface standing wave and X-ray photoelectron spectroscopic measurements. The influence of d-electron correlation on the predicted structures is briefly discussed, making use of the DFT + U scheme.

Keywords: Hematite; Vanadium adsorption; Surface oxidation; Density functional theory

1. Introduction

Growth and properties of ultra-thin metal films supported on metal oxides and the subsequent oxidization process form a very interesting research area, as they represent crucial steps to understand the observable structure and properties of heterogeneous metal oxide/metal oxide systems. Such heterogeneous interface structures have provided a novel class of materials that have enhanced catalytic properties compared to a single metal oxide. In addition, composition graded oxide interfaces are becoming very common in controlling electronic, optical, magnetic and thermal properties in complex artificial structures. Thus they have great potential in catalysis, gas sensing and environmental pollution control, microelectronics, optoelectronics, superconducting technology and high performance high temperature machines [1–3].

In this work we use the first-principles density functional theory (DFT) to study the submonolayer V adsorption on an α-Fe_2O_3 (hematite) (0001) surface and the subsequent oxidization process. Vanadium is a very versatile early transition metal element, as it can form various oxidization states (+3(d^2s^0), +5(d^0s^0) being most common) resulting in a wide range of chemical reactivity. Wide application of vanadium oxides has been found in the chemical industry:

* Corresponding author. Address: Department of Physics and Astronomy, Northwestern University, Evanston, IL 60208, United States. Tel.: +1 847 4913665; fax: +1 708 4919982.
E-mail address: don-ellis@northwestern.edu (D.E. Ellis).

0039-6028/$ - see front matter
doi:10.1016/j.susc.2007.05.028

supported vanadium oxide has attracted much interest in recent years as it has been found to possess enhanced catalytic properties; e.g., when supported by alumina, tin-oxide, ceria, titania, silica, and numerous other metal surfaces [4–6].

Hematite is also a very popular catalytic material, noted for its stability and abundance in the geochemical environment. However, its complex geometric and electronic structure, and interconvertability of various phases make fabrication of high quality atomically clean hematite surfaces challenging: experimental and theoretical characterizations of its surfaces and adsorption thereon have been very rare until recent years [7–10]. Experimental studies of V adsorption on clean hematite (0001) with subsequent repeatable oxidization-/reduction cycles were reported by Kim et al., using atomic resolved X-ray standing wave measurements (XSW) to detect V site geometry [11a] and X-ray photoemission spectroscopy (XPS) to detect electronic structure changes [11b]. Though considerable understanding is gained thereby for vanadium or vanadium oxide supported by hematite, to our knowledge no theoretical studies of the V/hematite or V_xO_y/hematite system have been made. Our level of understanding about such supported monolayer oxide potential catalysts can be enhanced by detailed theoretical modeling of surface composition and geometry, electronic density of states, oxidization state characterization, etc. The principal goal of the present work is to use DFT as a tool to explore and refine the proposed models based upon experiment, and to expand our knowledge of details of the underlying electronic structure.

The present work treats two interface structures: half monolayer (V/hematite), and stages of its oxidation (O_x/V/hematite), evaluated within the framework of spin-polarized DFT. In the first case we consider the adsorption of V on hematite (0001), with two idealized bulk-terminated surfaces, namely single-Fe terminated (Fe–O_3–Fe_2···) and oxygen-terminated (O_3–Fe_2–O_3···). Within each surface model, we obtain the energetically favorable adsorption sites by trying various starting scenarios and subsequently relaxing the structures. In addition to adsorption geometry and energy, we also obtain representations of the system's electronic structure including site-projected densities of states, charge distribution, core-region potential shifts, etc. In the second part of this work, we study the interaction of atomic oxygen with submonolayer V/hematite (0001). By studying the relaxed O adsorption structure, binding energy, and the resulting oxidation state changes of V and Fe, we hope to provide a good starting point for understanding the interface structure between vanadium oxide and hematite and its effects on chemical and catalytic properties.

Though the majority of this work is done within the conventional density functional theory, we note that considerable attention is paid to the influence of strong intra-atomic electronic correlations on physical properties of transition metal oxides. One of the popular methods of treating strong electronic correlation is the so-called DFT + U scheme that models intra-atomic correlation effects by adding an on-site Coulomb repulsion U to the DFT Hamiltonian [12–14]. Here, we also carry out some exploratory DFT + U calculations to investigate the impact of d–d correlation effects on adsorption energy and density of states of representative V/hematite systems.

Determining the favored adsorption sites and geometry for V on hematite is nontrivial, due in part to the inevitable disparity between clean ideal surfaces and the experimental environment. We thus encounter some conflict with experimentally derived structural models of Kim et al. [11a] and present a discussion of likely causes of the discrepancies.

The remainder of the paper is organized as follows: in Section 2, we introduce the computational methodology; Section 3 reports our results about V adsorption on both Fe- and O_3-terminated hematite (0001) surfaces; Section 4 reports our results for oxygen adsorption on V/hematite; Section 5 contains comments and discussion, and Section 6 gives our conclusions.

2. Computational methods

Spin polarized DFT calculations within a periodic slab model with plane wave basis sets were performed using the *Vienna Ab Initio Simulation Package* (VASP) [15–18]. The representation of ion-electron interactions is described by the projector augmented wave method (PAW) [19]. The electrons considered as core in the PAW potential are [1s2s2p3s] for vanadium (11 valence electrons/atom), [1s] for oxygen and for [... 2p3s] Fe (8 valence electrons/atom). Non-local corrections in the form of the spin-polarized generalized gradient approximation (GGA) as developed by Perdew, Burke and Ernzerhof (PBE) are adopted [20]. Automatically generated Monkhorst–Pack grids are used to carry out Brillouin zone integrations [21]. $4\times4\times1$ k-point meshes are chosen for the surface hexagonal unit cell in structural relaxation and energy calculations; k-point meshes of $8\times8\times1$ are chosen for calculation of densities of states (DOS). In self-consistent geometrical relaxation steps, a Gaussian-smearing finite temperature level-broadening method is used, of width $\sigma = 0.2$ eV; in energy calculations, the tetrahedron method with Blöchl corrections was used to do Brillouin zone sampling. To define geometry relaxation convergence we require that the force acting on relaxing atoms be smaller than 0.02 eV/Å. In a few exceptional cases we use a weaker criterion that neighboring geometry steps produce energy differences smaller than 1 meV/atom. Within the plane wave basis set we chose the cut off energy as 400 eV, which is sufficient according to previous experience with vanadium oxide and hematite VASP calculations [8,9].

A small number of calculations were carried out within the DFT + U method, using the form suggested by Liechtenstein and Dudarev et al. [12] and implemented in a PAW scheme by Bengone et al. [13] A detailed discussion of DFT + U implementation in VASP can be found in

Rohrbach et al. [14] The parameters and details of calculation will be presented in Section 3.

To model an idealized hematite (0001) surface, we use an asymmetric periodic slab whose x–y coordinates resemble those of bulk and whose z-direction includes a finite gap. The two idealized bulk terminations for our adsorption study: a single-Fe-terminated surface ($Fe^{S}_{A}O_3Fe^{S-1}_{C}Fe^{S-1}_{B}O_3-$) and full oxygen monolayer O_3-terminated surface ($O_3Fe^{S-1}_{C}Fe^{S-1}_{B}O_3Fe^{S-1}_{A}Fe^{S-1}_{C}-$) are illustrated in Fig. 1, with both side and top views. We use labels for each surface (S) or near-surface (S − 1) atomic layer, such as Fe^{S}, O_3, Fe^{S-1}, etc. We further distinguish the slab metal atoms that occupy octahedral Fe sites A, B, C by a subscript, as Fe^{S}_{A}, etc. Here site A indicates the occupied Fe site for single-Fe termination while site B indicates the unoccupied site which has a subsurface Fe directly below. Site C indicates the third octahedral site that is normally unoccupied, having a closer subsurface Fe directly below it. For the Fe-terminated surface, we choose a 12 atomic layer slab and for the O_3-terminated surface we choose an 11 layer slab. The thickness of the slab is thus about 8 Å and the chosen vacuum thickness between neighboring slabs is 15 Å. Previous calculations of hematite surfaces and convergence checks made in those works have proven that the slab and vacuum gap are both thick enough to minimize the slab–slab interaction and correctly account for the relatively large near-surface layer relaxation [7–9]. In the present calculations, lattice constants are fixed; all the ions are relaxed in three dimensions except for the five bottom layers in the slab, which are held rigid. We adopt dipole or quadrupole moment corrections in total energy and surface work function calculations but omit them in structure relaxation, as they play a very small role in deciding ground state structure.

The adsorption energy for V on hematite for different coverage was defined using the following formula:

$$E_{\mathrm{ads}} = \frac{1}{N}\left(E^{\mathrm{V/hem}}_{\mathrm{slab}} - E^{\mathrm{hem}}_{\mathrm{slab}} - NE^{\mathrm{V}}\right) \tag{1}$$

where negative E_{ads} means exothermic adsorption. $E^{\mathrm{V/hem}}_{\mathrm{slab}}$ is the total energy of the V covered single-Fe-terminated hematite slab, $E^{\mathrm{hem}}_{\mathrm{slab}}$ is the total energy of the clean hematite substrate slab, E^{V} is the energy of the isolated, spin-polarized V atom, and N is the number of adsorbed V per cell. Following convention, we suppress the sign of E_{ads} in the following tables and discussion. The coverage is defined as the ratio of the number of adsorbed vanadium atoms to the maximum number of metal atoms in an ideal substrate unit cell; i.e., 2 atoms/cell here. The work function change is calculated with the formula:

$$\Delta\Phi = \Phi^{\mathrm{V/hem}} - \Phi^{\mathrm{hem}} \tag{2}$$

where Φ is defined as the minimal energy required to remove an electron from the surface to vacuum. Concretely, it is calculated as the difference between vacuum electrostatic potential and the Fermi energy.

The adsorption energy of O is calculated by the formula analogous to Eq. (1):

$$E_{\mathrm{ads}} = \frac{1}{N}\left(E^{\mathrm{O/V/hem}}_{\mathrm{slab}} - E^{\mathrm{V/hem}}_{\mathrm{slab}} - NE^{\mathrm{O}}\right) \tag{3}$$

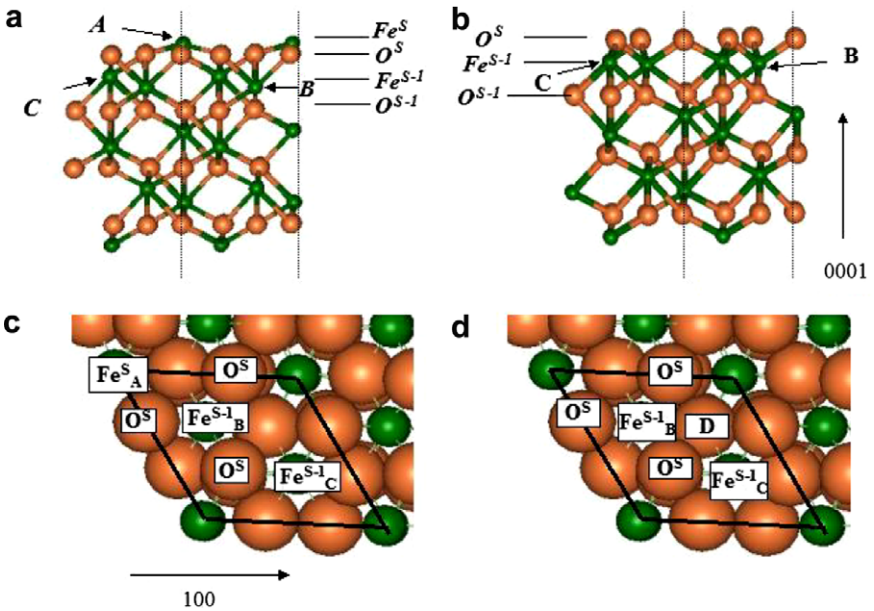

Fig. 1. Side and top views of the (0001) single Fe and O_3 terminated hematite surfaces. Fe atoms are smaller darker spheres and O atoms are larger lighter spheres. The threefold hollow sites A, B, C are pointed out in side view, along with the label of each atomic layer close to surface. For convenience of viewing, two unit cells are shown in side view, with distance between vertical dashed lines indicating the scale of single unit cell. In top view, the position of surface or subsurface Fe sites and surface O sites are shown within the 1×1 unit cell. In panel (d), we indicate site D, a further hollow site without Fe below.

$E_{slab}^{O/V/hem}$ is the total energy of the O–V/hematite complex, $E_{slab}^{V/hem}$ is the total energy of the selected V/hematite system we obtained in previous modeling, E^{O} is the energy of the isolated, spin-polarized O atom, and N is the number of adsorbed O per cell. The coverage is defined here as the ratio of the number of adsorbed vanadium atoms to the maximum number of hematite surface O atoms in an ideal substrate unit cell; i.e., 3 atoms/cell. It is becoming common to estimate thermodynamic stability of surface films and bulk solid solutions, making use of band structure energetics and approximate component chemical potentials. A particularly relevant example is the study of 1–6 layers of V_nO_m supported on α-Al_2O_3 (0001) by Todorova et al. [22] where the changes in Gibbs surface free energy were approximated as

$$\Delta\gamma(T,p) = [\Delta E - n\Delta\mu_V - m\Delta\mu_O] \quad (4)$$

The changes in chemical potential $\Delta\mu_i$ were taken from ideal gas behavior for O_2 and bulk thermodynamic data for vanadium. Vibrational entropy and other configurational terms were considered to be negligible. The authors were thus able to explore the range of stability for varying film thickness and composition. In the present work the V concentration n is fixed, and m varies over 1/3, 2/3, and 1 monolayer oxygen coverage. Plots of $\Delta\gamma(T,p)$ thus resolve to three straight lines on a graph vs. $\Delta\mu_O$ which indicate increasing stability up to 1 ML oxygen, as would be expected since the V coordination sphere is otherwise incomplete.

The atomic resolved partial density of states (PDOS) is calculated by projecting the calculated wave functions onto their spherical harmonic components inside specified atomic spheres. The radius of such spheres is denoted as R_S. We chose R_S for Fe as 1.3 Å, for V as 1.2 Å, and for O as 0.8 Å. In calculating electronic populations of each atom, both Bader analysis algorithms and a straightforward volume charge integration within R_S are adopted. The Bader analysis is based on a scheme suggested in Henkelman et al. and implemented in their ''Bader Charge Analysis'' program [23]. It provides a space-filling ''topological atom'' measure of atomic charge quickly and robustly. Of course, any volume charge integration consists of a selected nonunique charge partitioning. The results can be non-intuitive, especially for systems with large covalent bonding character. However, it does provide a lot of detailed information about the population of valence electron orbital and their variation with spatial location, which can be interpreted as chemical state changes. In the present work a comparison between R_S volume integration and Bader charge is especially helpful, since we are able to detect interorbital charge transfers which move charge from inside R_S (e.g., V 3d) to more diffuse regions (e.g., V 4sp) and vice versa. such changes reflect subtle but important rearrangements of electronic structure which would be missed in a single analysis framework.

In treating V adsorption/oxidation on hematite, we also examine transition metal core level shifts; this is useful in associating our geometry and electronic structure calculations with what can be directly measured in XPS experiments. Careful theoretical interpretation of core shifts is necessary, since the core hole represents a major perturbation on the system of interest. The so-called initial state approximation omits electronic screening effects from valence electrons as the core electron is excited; therefore, it only describes core level shifts semi-quantitatively, nevertheless providing a useful probe of the ground state potential. More rigorous transition- and final-state approximations are most conveniently treated in an embedded cluster framework; however, periodic supercell calculations with one core-hole per unit cell can also be useful [22]. In the cluster calculations an isolated hole is treated; in periodic calculations one core electron per cell is transferred to the Fermi level to maintain overall neutrality, and Coulomb hole–hole interactions from one cell to another are a concern. The magnitude of screening effects clearly varies in different systems, Methfessel et al. [24a] examined MgAu alloys, pointing out the value of initial-state analysis and its limitations, and the difficulty of using any simplified approximations. For example, the initial-state approximation for Mg 1s is even of the wrong sign, while the Au 4f screening effects are very small. The detailed implementation of core level shift calculations is described elsewhere [24b]. Most of our results are given in the initial state approximation based on the VASP ground state potential; however, we will examine one surface site further, using cluster methods.

The first principles local-density self-consistent-field (SCF) embedded-cluster method also used in this work, applies the SCF local-density theory in a molecular-orbital (MO) framework to describe electronic properties of solids [25–27]. The linear combination of atomic orbitals (LCAO) method and discrete variational method (DVM) with a numerical integration scheme was used, with atomic radial basis functions generated as numerical solutions of atoms/ions in a potential well represented by values tabulated on a net of points. The effective atomic configurations of the cluster atoms are obtained self-consistently by iterating the charge and spin density, using the Vosko–Wilk–Nusair (VWN) exchange and correlation potential [27] and a least-squares fit of model parameters to the eigenvector densities [26]. While the PBE functional, with its Generalized Gradient Approximation is very suitable for structural optimization using the plane wave VASP band code, we have greater confidence and experience (and a plentiful literature) in interpretation of VWN functional results for electron distributions in the context of molecular clusters with an LCAO basis. In any event we would expect differences between PBE and VWN charges densities to be small, within a given basis set and computational scheme. As to the embedding model, the charge density ρ that determines both Coulomb potential and the approximate exchange-correlation potential V_{xc} includes contributions from the embedding lattice as well as the variational cluster [28]. Thus, the total Coulomb potential can be written as

$V_C^{tot} = V_C^{clust} + V_C^{emb}$, where V_C^{emb} is the Coulomb potential contributed by the assumed charge distribution of embedding lattice calculated by Ewald summation [29]. V_{xc} is determined as a functional of the total density as well.

In the electronic structure studies by the cluster method, we extract bond orders (BO), which evaluate the degree of shared charge between atoms. These can be defined as the summation of overlap populations between atoms μ and v, multiplied by appropriate density matrix components

$$BO_{\mu,v} = \sum_{i\ni\mu, j\ni v} S_{ij} \sum_k n_k C_{ik} C_{jk} \quad (5)$$

Here S is the overlap matrix between basis functions, n_k are occupation numbers for eigenstates k, and C is the matrix of variational expansion coefficients. BO provides an index reflecting strength of covalent bonds. In the same spirit, we also give a Mulliken population analysis that will be useful for understanding electron transfer between adjacent atoms.

In our charge density maps, we extract another bonding index that is the value of density on a bond-line at the inter-atomic surface (where the gradient of the charge density $\nabla\rho = 0$), a so-called 'bond critical point (ρ_c)' [30]. This concept helps to define a 'topological atom' as mentioned earlier in ''Bader Analysis'' of periodic slab calculation and reflects the covalency at the inter-atomic surface.

Using relaxed structures resulting from the periodic slab models, we carried out trials to optimize cluster computational parameters, which included integration meshes for SCF and total energy calculations, convergence of density and potential with SCF iterations, convergence of charge density with respect to size and composition of variational bases for wavefunctions and density expansions, etc. Details and setting of computational parameters are described elsewhere [31,32], only essential data will be given here. The variational clusters are generated from the well-relaxed geometry obtained by VASP. After considering the balance of accuracy and cost, the cluster sizes are chosen to include 35–50 atoms, surrounding atoms of interest in such a way that the cluster boundary effects can be mostly neglected. For local chemical bonding considerations, we find that we can omit the embedding density altogether. This approximation would not be adequate for treatment of binding energies or atomic forces, which was not the main purpose of cluster calculation in this work. The SCF iterations are carried to a convergence of both charge and spin to 10^{-3} e. By comparing the data before (clean) and after V-adsorption, we will see clearly the effects of adsorption on the substrate. Since orbital-based analyses depend upon the expansion basis, it is important to make relative comparisons and to extract trends, rather than to interpret absolute values. Indeed, due to different methodologies used, we cannot expect to directly compare density analyses from VASP (plane wave, periodic) and DVM (LCAO, cluster); however, common features will be reinforced.

3. Results: V adsorption on hematite (0001) surface

As shown in Fig. 1, there are several possible V adsorption sites: for single Fe-terminated hematite (0001) these include: (1) Threefold hollow B which has a subsurface Fe_B^{S-1} atom below; (2) threefold hollow C which has a subsurface Fe_C^{S-1} atom that is higher than Fe_B^{S-1}; (3) the bridge site between two surface O atoms; (4) direct on-top of surface Fe_A^S; (5) direct on top of surface O; (6) substitution of V for Fe_A^S, while Fe_A^S displaces to other sites such as B and C. For an O_3-terminated surface, adsorption sites considered are top adsorption on O, and threefold hollow sites A, B, C plus the fourth threefold hollow site D, having no subsurface Fe (see Fig. 1).

As an initial step we carried out relaxation calculations for both Fe-terminated and O_3-terminated surface slabs. As expected, we obtain very similar results to those obtained in previous DFT modeling of hematite surfaces in terms of structure, work function and local magnetic moment. For example, the most significant relaxation effect for the single-Fe terminated surface is the contraction of first and second interlayer distances and a flattening trend for the cations Fe_C^{S-1} and Fe_B^{S-1} within the near surface metal layers. Details may be found in Refs. [7–9]; for convenience in comparison with the following, a summary of pure hematite slab results is given in Table 1. The reader may be reminded that the Fe magnetic moment is considerably underestimated, which is a common problem associated with approximate GGA treatment of strong electronic correlations. The geometric structure is better approximated as it is mainly decided by electrostatic interactions [9]. The work functions calculated for the idealized model surfaces are 4.0 eV for Fe-termination and 7.6 eV for O_3-termination, similar to the results of Wang et al. [7] with a full-potential linearized augmented plane wave (FP-LAPW) periodic slab model. The Fe-terminated surface workfunction result differs from that obtained in cluster calculations of Batista and Friesner [33], whose predicted value is 5.6 eV. We suppose the source of this discrepancy may be primarily a cluster-size effect, since the work-function results from fairly sensitive long-range interactions.

3.1. 0.5 ML V/Fe–hematite interface

3.1.1. Adsorption site, geometry and energy

For 0.5 ML V/Fe–hematite, our calculations imply that among all sites examined, only adsorption on threefold hollow site configurations and V directly adsorbed on Fe_A^S are stable. For other initial configurations, for example, starting from a local-minimum-energy geometry of V on top of O, further optimization will cause V to dislocate to form bonds with two additional O or with one surface Fe atom. Likewise, V initially adsorbed at the O-bridge position slides into a nearby threefold hollow site.

A summary of adsorption energy and work function changes for all stable scenarios found in 0.5 ML V adsorption is given in Table 2, where we can see that all three

Table 1
Surface relaxation, work function and local magnetic moment for Fe-terminated and O_3-terminated hematite

Termination	Fe^S–O^S	O^S–Fe^{S-1}	Fe^{S-1}–Fe^{S-1}	Fe^{S-1}–O^{S-1}	O^{S-1}–Fe^{S-2}
(a) Relaxation					
···Fe[a]	−51.3%	6.4%	−31.7%	13.1%	–
···Fe[b]	−59.4%	5.8%	−46.0%	9.7%	–
···O_3[a]	–	−4.9%	−78.4%	34.7%	−7.1%
···O_3[b]	–	−5.8%	−73.0%	30.6%	4.5%
			···Fe		···O_3
(b) Work function (eV)			(4.3[c]) 4.0[d]		(7.6[c])7.6[d]
	Fe^S	O^S	Fe^{S-1}	O^{S-1}	Fe^{S-2}
(c) Magnetic moment for surface region atoms (μ_B)					
···Fe[e]	3.3	0.0	−3.5	0.0	–
···Fe[f]	3.4	0.0	−3.5	0.0	3.5
···O_3[e,g]	–	−0.2	−1.7	0.1	−3.6
···O_3[f]	–	−0.2	−1.7	0.1	3.6

The relaxation is given as percentage change of interlayer distances along the (0001) direction relative to those in bulk.
[a] Ref. [8].
[b] This work.
[c] Ref. [7].
[d] This work.
[e] Ref. [8].
[f] This work.
[g] For O_3-termination, we change the sign of Fe ions reported in [8] to maintain the consistency among different terminations.

hollow site adsorptions imply large binding energies of 5–6 eV, due to the formation of three V–O bonds between adsorbate and surface. V adsorption on top of Fe, though metastable in our calculation, implies very low adsorption energy of 1.5 eV. The most stable case found is (V_B, Fe_A^S) with E_{ads} of 6.2 eV, about 0.8 eV higher than the next most favorable configurations. For this structure, the work function shows a very small decrease of 0.22 eV, and for the remaining configurations the work function drop is similarly small. (V_C, Fe_B^S) is an exceptional case in which the work function increases by 0.4 eV.

Our results for adsorption geometry change upon 0.5 ML V adsorption are illustrated in Table 3a. There are significant bonding geometry differences: the site arrangements significantly affect the equilibrium V–O bond length and subsequently, the adsorption energy. For instance, in the most stable configuration (V_B, Fe_A^S), V can approach O closely without encountering too large a repulsion with the Fe_B^{S-1} below. In this configuration, the V–O bond length is 1.76 Å and the vertical distance of V from the O plane is less than 0.1 Å. Also, the distance between V_B and Fe_B^{S-1} is only 2.56 Å, which indicates a V–Fe covalent interaction, analyzed in detail below.

3.1.2. Electronic and bonding properties

The metal 3d and O 2p atom-resolved DOS for a clean Fe-terminated hematite surface and 0.5 ML V_B/Fe–hematite can be found in Fig. 2. The DOS is broadened using a Gaussian function, with width of 0.2 eV for easy viewing. For clean Fe-terminated hematite, the DOS is qualitatively similar to that obtained by Rohrbach et al. [9]. There is strong hybridization between surface/near surface Fe 3d and O 2p orbitals. From −8 eV to −2 eV (with respect to the Fermi energy E_f), the bound-state region DOS is dominated by the broad O 2p band with sizable bonding contributions from majority spin Fe 3d orbitals. From −2 eV to above E_f, the DOS is dominated by Fe 3d character. We recall that the most stable structure is antiferromagnetic, with alternating up, down spins in successive Fe layers.

Upon 0.5 ML V adsorption, the most significant change of Fe 3d DOS is the downward shift of some peaks originally above E_f, for both Fe^S and Fe^{S-1} atoms. Another notable change is that the DOS for Fe^S gets significantly sharper; i.e., more atomic-like, presumably because the weaker Fe–O bonding causes the effective coordination number around Fe to decrease. For O 2p bands, we can see that the DOS increases in the high binding energy region (∼8 to 5 eV below E_f) while decreasing at low binding energy (∼−2.5 eV). The energy overlap of the O 2p band with Fe_B^{S-1} is a little bit misleading since their bond is broken; a very significant sign of such bond breaking is the appearance of a spin up peak for Fe_B^{S-1} at around −2 eV. The hybridization between O 2p and Fe_A^S and Fe_C^{S-1} at high binding energy is apparently weakened by V adsorption. The V contribution is divided approximately into three parts, a high binding energy valence band from −8 eV to −3 eV, a low binding energy band from −3 eV to −1 eV, and a non-bonding conduction band from −1 eV to above E_f. Electrons in the bonding region are mostly spin up, while non-bonding electrons are mostly spin down. In spite of the existence of surface Fe, this DOS is qualitatively similar to what is obtained for a pure V_2O_3 (0001) surface [34,35].

Table 2
Adsorption energy E_{ads} and work function change $\Delta\Phi$ for 0.5 ML V/Fe–hematite, V/O_3–hematite, O/V/Fe–hematite, and O/V/O_3–hematite

Adsorption site	E_{ads} (eV/atom)	$\Delta\Phi$ (eV)
(a) Adsorption energy		
0.5 ML V/Fe		
TOP(Fe)	−1.54	−1.10
TOP(O)	Unstable	–
BR(O–O)	Unstable	–
TH(V_C, Fe_A^S)	−4.92	−0.49
TH(V_A, Fe_C^S)	−5.18	−0.04
TH(V_B, Fe_A^S)	−6.20[b]	−0.22
TH(V_A, Fe_B^S)	−5.44	−0.20
TH(V_B, Fe_C^S)	−5.32	−0.30
TH(V_C, Fe_B^S)	−4.80	0.42
0.5 ML V/O_3		
TOP(O)	Unstable	–
TH(V_A)	−9.91	−3.75
TH(V_B)	−9.27	−4.45
TH(V_C)	−7.54	−4.47
TH(V_D)	−9.19	−3.59

$U - J$ (eV)	0.0	1.0	2.0	3.0
(b) GGA + U results for ML V_B/Fe–hematite				
E_{ads} (eV)	−6.20	−5.11	−4.21	−2.99

0.5 ML V/Fe	0.5 ML V/O_3
(c) Adsorption energy for VO_x–hematite	
1/3 ML O	
O_b	−7.40 –
O_t on Fe	−4.55 –
O_t on V	−6.70 −6.56
2/3 ML O	
O_b	−6.62 Unstable
O_t	−5.52
1 ML O	
O_b	−6.01 Unstable

"TOP" site means V atom is initially put on top of surface atom (the bracket indicates the type); "BR" site means V is initially put at bridge site; "TH" sites mean threefold hollow site among three O atoms. O_b indicates the adsorbed O forming a bridging bond with metal atoms. O_t indicates adsorption directly on top of a metal. The site labels of V and Fe indicate different initial adsorption configurations examined, as explained in the text. Where an adsorption energy is listed, the site is locally stable.

Table 4 summarizes our calculations for the electronic configuration of Fe–hematite and V/Fe–hematite. Fe_2O_3 and V_2O_3 reference states were calculated in the corundum structure with lattice constants ($a = b$, c) of (5.04, 13.73) Å and (4.94, 13.97) Å, respectively. FeO and VO reference states were calculated in the rock salt structure with lattice constants of 4.33 Å and 4.08 Å, respectively. Orthorhombic V_2O_5 was calculated with lattice constants $(a, b, c) = (11.51, 3.56, 4.37)$ Å. The vanadium compounds were treated as non-spin polarized. Estimating atomic charge by Bader analysis for 0.5 ML V adsorption, we found a population increase for Fe_A^S, Fe_C^{S-1} and Fe_B^{S-1}, (0.39 e, 0.17 e, 0.52 e) compared to the clean surface; after charge redistribution upon V adsorption, Fe_A^S and Fe_B^{S-1} are thus partially reduced. Comparing to reference states for Fe^{3+} and Fe^{2+} calculated for bulk compounds shown in the Table, Fe_A^S and Fe_B^{S-1} have an oxidization state smaller than 2+. For V, the Bader analysis gives charge of +1.62 e, somewhere between V^{3+} and V^{2+} states. The R_S volume charge integration for V_B gives 0.98 e, with 3.32 e assigned to d orbitals; i.e., an increase over the free V^{3+} state due to V_{3d}–O_{2p} covalency. According to R_S volume charge integration, Fe_A^S experiences a minor decrease of net charge, from +0.85 e in clean surface to +0.76 e after V adsorption, the s and p electrons decreasing by 0.16 e while d electrons increase by 0.24 e. Meanwhile, the net charge of Fe_C^{S-1} increases by 0.25 e, with a decrease in s and p electrons and no change in d electrons. For Fe_B^{S-1}, the ionicity decreases by 0.31 e, with d electrons increasing by 0.21 e; this is likely due to the direct "covalent" interaction between Fe_B^{S-1} and V_B. Fe_A^{S-2} also shows a small decrease in ionicity. Turning now to the Bader analysis, where electrons are counted inside a flexible ($\nabla\rho = 0$) surface we note a consistent decrease in ionicity for all Fe sites, with Fe_A^S and Fe_B^{S-1} being most strongly reduced by this measure. As noted previously, the different sampling conditions for R_S integration and Bader analysis allow us to detect interorbital transfers and details of electronic rearrangement (e.g., for Fe_C^{S-1}) that no single scheme could provide. Finally, upon V adsorption, the surface Fe_A^S magnetic moment decreases from 3.3 μ_B (clean surface) to 2.9 μ_B; V_B has a small moment of −0.6 μ_B. The magnetic moment changes for subsurface Fe are very small.

Table 5 gives a summary of Mulliken populations, charge, spin, and bond orders obtained from SCF cluster results. In the 0.5 ML V/Fe–hematite case, the nearby Fe_B^{S-1} is found to share considerable charge with adsorbed V, with bond order of 0.39 e and Mulliken charge reduced by 0.69 e, being the most affected substrate atom. Fe_A^S and Fe_C^{S-1} are also slightly reduced: by 0.11 and 0.05 e according to volume charge. It can thus be seen that this V adsorption involves significant charge sharing, rather than straight-forward ionic Coulomb interaction. To further clarify the bonding character, we give charge density contour maps of 0.5 ML V/Fe–hematite, plotted by projecting the charge density onto a bond-containing plane shown in Fig. 3. The bonding contours, when compared with those of a clean surface, indicate clearly that O^S–Fe_B^{S-1} bonding is greatly weakened, while there is bond formation between adsorbed V and Fe_B^{S-1}. We measured the bond critical-point charge that, as mentioned above, reflects the covalent bond strength, according to Bader's topological theory of atoms. The present example shows a ρ_c of 0.056 e/a_0^3 for the V–Fe_B^{S-1} bond, comparable to the value of 0.089 for the V–O bond, further verifying the considerable V–Fe_B^{S-1} covalent character due electron-sharing between V 3d and Fe 3d orbitals.

3.1.3. Core level shift

Table 6 lists core level shifts calculated in the initial state approximation using the VASP periodic potential; all Fe values are given with reference to the same atoms' core binding energy before V adsorption. A negative value

Table 3
Adsorption geometry of hematite, V/Fe–hematite, V/O_3–hematite, O/V/Fe–hematite and $O/V/O_3$–hematite

Sites	Clean slab	V_C, Fe^S_A	V_A, Fe^S_C	V_B, Fe^S_A	V_A, Fe^S_B
(a) Clean hematite surface and 0.5 ML V/Fe–hematite					
Inter-atomic distance (Å)					
$V–Fe^S$	–	2.85	2.94	2.95	2.89
$V–O^S$	–	1.85	1.80	1.76	1.78
$Fe^S–O^S$	1.79	1.82	1.90	1.86	1.87
$O^S–Fe^{S-1}_C$	1.90	2.06	2.05	2.08	2.08
$O^S–Fe^{S-1}_B$	2.08	2.51	2.43	3.05	2.70
$V–Fe^{S-1}_{B/C}$	–	2.74	–	2.56	–
$Fe^S–Fe^{S-1}$	–	–	2.76	–	2.50
Interlayer distance (Å)					
$V^S–O^S$	–	0.77	0.43	0.07	0.61
$Fe^S–O^S$	0.39	0.37	1.06	0.67	0.49
$O^S–Fe^{S-1}$	0.90	1.55	1.46	1.41	1.39
$Fe^{S-1}–Fe^{S-1}$	0.44	0.01	0.08	1.08	0.62
$Fe^{S-1}–O^{S-1}$	0.95	1.03	1.00	0.32	0.69

	Clean slab	$V_A–O_3$	$V_B–O_3$	$V_C–O_3$	$V_D–O_3$
(b) Clean O_3–hematite surface and 0.5 ML V/O_3–hematite					
Inter-atomic distance (Å)					
$V–O^S$	–	1.73	1.70	1.75	1.72, 1.75, 1.76
$O^S–Fe^{S-1}_C$	1.77	2.03	1.97	2.15	1.90
$O^S–Fe^{S-1}_B$	1.79	2.19	2.62	2.00	2.43
$V–Fe^{S-1}_{B\text{ or }C}$	–	–	2.51	2.13	2.45, 2.72
Interlayer distance (Å)					
$V–O^S$	–	0.46	0.47	0.70	0.49
$O^S–Fe^{S-1}_C$	0.81	1.10	1.15	1.43	1.10
$Fe^{S-1}_C–Fe^{S-1}_B$	0.14	0.35	0.89	0.15	0.37
$Fe^{S-1}_B–O^{S-1}$	1.13	0.95	0.56	1.07	0.84

Coverage/bond length (Å)	O–V	O–Fe^S	V–O^S	$Fe^S–O^S$	$O^S–Fe^{S-1}$	V–Fe^{S-1}
(c) 1/3, 2/3 and 1 ML O on 0.5 ML V/Fe–hematite: bond length and interlayer distance						
1/3 ML O	1.74	1.92	1.83	2.04	2.23/2.17/2.01	2.79
			1.80	1.95	2.08/3.07/4.22	
			1.76	1.92		
2/3 ML O	1.67/1.71	1.92/2.02	1.79	1.86	1.91/2.02/2.08	–
			1.95	1.93	2.07/2.30/2.37	
			2.36	2.11		
1 ML O	1.74	1.86	2.13	1.96	1.96	–
					2.22	

Interlayer distance (Å)	$O_{ads}–O^S$	V–O^S	$Fe^S–O^S$	$O^S–Fe^{S-1}$	$Fe_B{}^{S-1}–Fe_C{}^{S-1}$	$Fe^{S-1}–O^{S-1}$
Before O_{ads}	–	0.07	0.67	1.41	1.08	0.62
1/3 ML O	2.02	0.60	0.82	1.28	0.89	0.51
2/3 ML O	2.19/2.26	1.25	0.91	1.01	0.58	0.80
1 ML O	2.09	1.45	1.01	0.82	0.59	0.76

Coverage/bond length (Å)	O–V	V–O^S	$O^S–Fe^{S-1}$	$V^S–Fe^{S-1}$
(d) 1/3 ML O on 0.5 ML V/O_3–hematite				
1/3 ML O	1.61	1.81	1.93 2.12	–

Coverage/Interlayer distance (Å)	$O_{ads}–O^S$	V–O^S	$O^S–Fe^{S-1}$	$Fe^{S-1}–Fe^{S-1}$	$Fe^{S-1}–O^{S-1}$
Before O_{ads}	–	0.46	1.10	0.35	0.95
1/3 ML O	2.31	0.71	0.93	0.39	1.01

For inter-atomic bonding distance or interlayer distance A–B, the following rule expresses the multiple values: when A varies (for example, more than one adsorbed O atom), then "/" is used to distinguish different values, when B varies (for example, different Fe^{S-1}), then different lines are used to distinguish different values.

normally means that the atom is being reduced while positive values generally suggest oxidization. The V core level shift is given relative to V^{3+} calculated in bulk V_2O_3. For 0.5 ML V adsorption, we observe that there is a very large shift of −0.68 eV for Fe^S_A while the subsurface Fe only have small shifts of about −0.3 eV. It is surprising to see that the

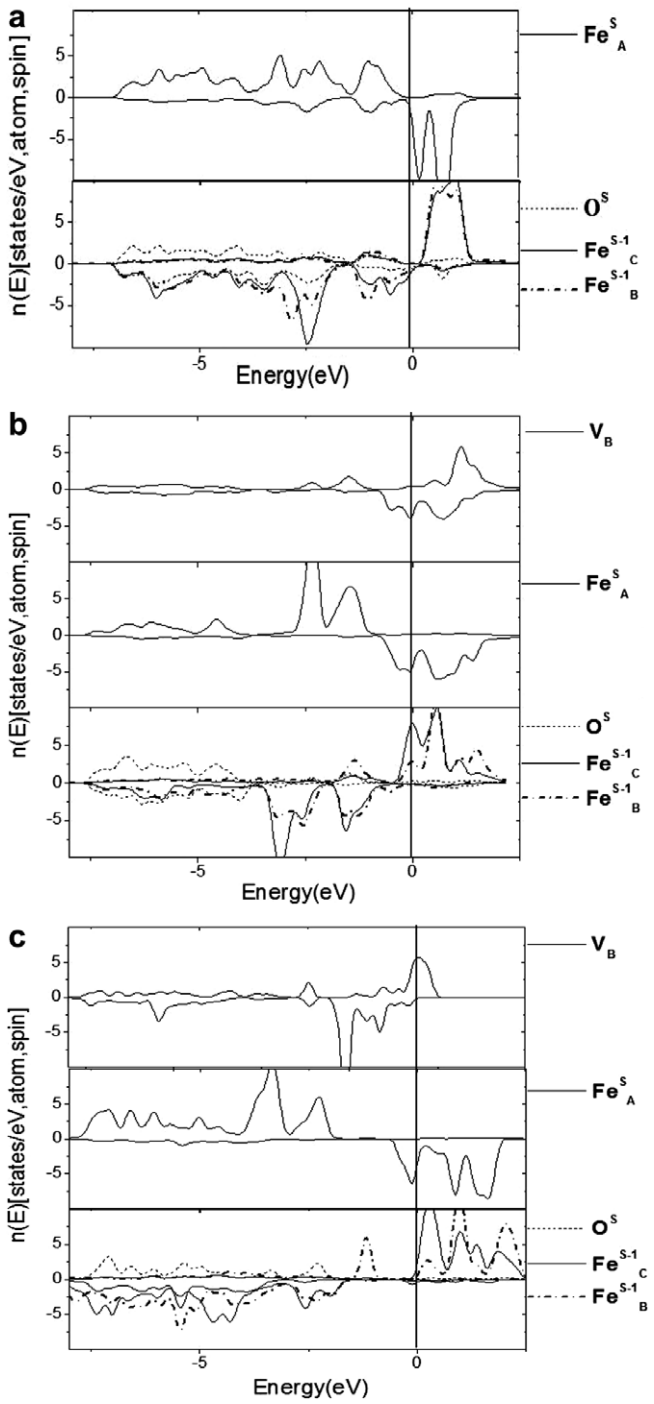

Fig. 2. Atom-resolved DOS for (a) clean Fe-terminated hematite (0001), (b) 0.5 ML V_B-hematite, (c) 0.5 ML V_B/Fe–hematite in GGA + U scheme with $(U, J) = (4.00, 1.00)$ eV. Positive value indicates spin up electronic states while negative indicates spin down. For V and Fe, only 3d electronic states are shown and for O, 2p states are shown. Fermi energy is fixed at 0 eV. The same rule applies for the remaining DOS figures in this work.

more deeply buried Fe_A^{S-2} incurs a +0.25 eV shift after V adsorption, though the Bader charge and R_S volume charge are unchanged. This indicates that potential shifts have long range electrostatic components which extend beyond local integration volumes. Adsorbed V has a zero core level shift compared to V^{3+}, confirming its 3+ state.

3.1.4. Intra-atomic correlations: GGA + U

We used the GGA + U method (implemented in VASP) to estimate the effects of d–d correlation on adsorption energy, limiting our study to the 0.5 ML V_B/Fe–hematite case. Due to limitations for computing resources and time, we did not use GGA + U to relax the geometry, as GGA + U has been found to play a small role in surface relaxation [9]. Instead, we used relaxed geometry obtained by the GGA method, choosing different U ranging from 1 to 4 eV (J is held constant as 1 eV) for both V and Fe. The U–$J = 1$ eV limit represents the scenario without onsite Coulomb repulsion, while U of 4 eV represents a probable overestimation of onsite Coulomb correlation. Due to the lack of detailed experimental information about adsorption energy and geometry, currently it is not feasible to identify an optimal U value for our V/Fe–hematite system. The major goal here is to find the correlation between applied U value and consequent calculated adsorption energy, densities of states, oxidization state change, etc. As shown in Table 4, it is found that approximately, 1 eV increase for U will result in a 1 eV decrease on V_B adsorption energy. The Bader charge analysis for the V_B/Fe-structure across different U implies very minor change, of a few hundredths of an electron charge. This implies that the transition metal oxidization state depends little on 3d–3d electron correlation, which would be expected if the main effect is to open a gap between energies of occupied and vacant states. However, we can see some effects, using R_S volume charge integration: when U–J reaches 2.0 eV, there is significant population increase in d electrons for V_B and population decrease for Fe_C^{S-1}. For other Fe atoms, U has very little effect on the volume charge integration and individual orbital character. The different perspectives held by Bader analysis and volume charge integration thus permit us to understand the effects of U in more detail. The application of U has some expected significant effects on DOS, as illustrated in Fig. 2 for $U = 4.0$ eV, resulting in the downward shift of Fe's anti-bonding orbitals, and a gap arising within the antibonding/non-bonding area. The V_B orbital distribution has very little change except for a shift towards higher binding energy.

3.2. 0.5 ML V/O_3–hematite interface

3.2.1. Adsorption site, geometry and energy

Here we discuss results for 0.5 ML V adsorption on O_3-terminated hematite. The most stable adsorption configuration is found to be the threefold A site; details are collected in Table 2. At this site V can avoid repulsive interaction with the sub-surface Fe^{S-1} atom directly below, while forming strong V–O bonds and compensating the excess surface negative charge, resulting in very large adsorption energy of 9.9 eV. Sites B and D also have comparable adsorption energies of 9.3 eV and 9.2 eV, respectively; again V_B and V_D only have minor interactions with nearby Fe atoms. For the V_A configuration, the surface work function decreases considerably by 3.75 eV; the

Table 4
Electronic net charge and population analysis and magnetic moments for reference bulk compounds and surfaces: Fe–hematite, V/Fe–hematite, O_3–hematite, V/O_3–hematite, O/V/Fe–hematite and O/V/O_3–hematite derived from band structure calculations

Site	R_S volume charge (e)	Bader charge (e)	Magnetic moment (μ_B)
(a) V/Fe–hematite charge			
Reference bulk compounds			
Fe^{2+}(FeO)	+1.24(0.29,0.36,6.11)	+1.44	3.5
Fe^{3+}(Fe_2O_3)	+1.77(0.23,0.29,5.71)	+1.79	3.7
V^{2+}(VO)	+1.52(0.18,6.16,3.14)	+1.44	0
V^{3+}(V_2O_3)	+1.47(0.26,6.28,3.00)	+1.86	0
V^{5+}(V_2O_5)	+1.07(0.39,6.43,3.11)	+2.25	0
Clean Fe–hematite			
Fe_A^S	+0.85(0.43,0.59,6.14)	+1.61	3.4
Fe_C^{S-1}	+1.03(0.39,0.58,6.00)	+1.81	−3.5
Fe_B^{S-1}	+1.17(0.36,0.52,5.95)	+1.81	−3.5
Fe^{S-2}	+1.14(0.36,0.52,5.98)	+1.78	3.5
0.5 ML V/Fe			
V_B	+0.98(0.37,6.33,3.32)	+1.62	−0.6
Fe_A^S	+0.76(0.38,0.48,6.38)	+1.22	2.9
Fe_C^{S-1}	+1.28(0.31,0.41,5.99)	+1.64	−3.5
Fe_B^{S-1}	+0.86(0.44,0.55,6.16)	+1.29	−3.2
Fe_A^{S-2}	+1.11(0.37,0.53,5.99)	+1.76	3.5

	$U-J=0.0$ eV	$U-J=1.0$ eV	$U-J=2.0$ eV	$U-J=3.0$ eV
(b) V/Fe GGA+U				
E_{ads} (eV)	6.20	5.11	4.21	2.99
Bader analysis				
V_B	+1.62	+1.63	+1.69	+1.62
Fe_A^S	+1.22	+1.24	+1.28	+1.30
Fe_C^{S-1}	+1.64	+1.65	+1.63	+1.79
Fe_B^{S-1}	+1.29	+1.31	+1.31	+1.39
Fe_A^{S-2}	+1.76	+1.81	+1.85	+1.87
R_S volume integration analysis				
V_B	+0.98(0.37,6.33,3.32)	+0.91(0.37,6.34,3.38)	+0.57(0.39,6.34,3.70)	+0.85 (0.38, 6.34, 3.43)
Fe_A^S	+0.76(0.38,0.48,6.38)	+0.90(0.38,0.48,6.24)	+0.82(0.39,0.49,6.30)	+1.14 (0.38, 0.48, 6.01)
Fe_C^{S-1}	+1.28(0.31,0.41,5.99)	+1.37(0.31,0.42,5.90)	+1.73(0.31,0.41,5.55)	+1.87 (0.31, 0.42, 5.39)
Fe_B^{S-1}	+0.86(0.44,0.55,6.16)	+0.86(0.45,0.55,6.14)	+0.84(0.45,0.56,6.14)	+1.02 (0.46, 0.56, 5.97)
Fe_A^{S-2}	+1.11(0.37,0.53,5.99)	+1.10(0.37,0.54,5.98)	+1.14(0.38,0.55,5.94)	+1.15 (0.38, 0.56,5.92)

	R_S charge (e) Q (s, p, d)	Bader charge (e)	Magnetic moments (μ_B)
(c) V_A/O_3 charge			
Clean O_3–hematite			
Fe_C^{S-1}	+0.51(0.49,0.78,6.22)	+1.87	−1.7
Fe_B^{S-1}	+0.66(0.46,0.71,6.17)	+1.85	−1.7
Fe_A^{S-2}	+1.16 (0.37,0.52,5.95)	+1.81	3.6
0.5 ML V_A/O_3–hematite			
V_A	+1.11(0.36,6.33,3.20)	+1.59	0.8
Fe_C^{S-1}	+1.16(0.35,0.49,6.00)	+1.72	−3.6
Fe_B^{S-1}	+1.21(0.34,0.47,5.98)	+1.72	−3.6
Fe_A^{S-2}	+1.12(0.37,0.52,5.99)	+1.77	3.6

	R_S volume charge (e) Q (s, p, d)	Bader charge (e)	Magnetic moments (μ_B)
(d) O/V/Fe–hematite charge			
1/3 ML O/0.5 ML V_B/Fe–hematite			
V_B	+1.02(0.37,6.41,3.20)	+1.99	0.0
Fe_A^S	+1.02(0.36,0.47,6.16)	+1.45	3.3
Fe_C^{S-1}	+1.31(0.30,0.40,5.99)	+1.60	−3.5
Fe_B^{S-1}	+0.93(0.40,0.43,6.14)	+1.48	−3.2
2/3 ML O/0.5 ML V_B/Fe–hematite			
V_B	+0.99(0.39,6.42,3.20)	+2.12	0.1
Fe_A^S	+1.01(0.38,0.55,6.07)	+1.69	3.5
Fe_C^{S-1}	+1.17(0.34,0.49,6.00)	+1.71	−3.4
Fe_B^{S-1}	+1.11(0.36,0.51,6.02)	+1.71	−3.5

(*continued on next page*)

Table 4 (*continued*)

Site	R_S volume charge (e) Q (s, p, d)	Bader charge (e)	Magnetic moments (μ_B)
1 ML O/0.5 ML V_B/Fe–hematite			
V_B	+1.16(0.36,6.41,3.07)	+2.20	−0.1
Fe_A^S	+0.64(0.43,0.70,6.22)	+1.84	1.4
Fe_C^{S-1}	+1.21(0.36,0.52,5.90)	+1.85	−3.7
Fe_B^{S-1}	+1.26(0.35,0.47,5.92)	+1.77	−3.7
1/3 ML O/0.5 ML V_A/O_3–hematite			
V_A	+1.00(0.39,6.42,3.20)	+2.19	−0.2
Fe_C^{S-1}	+1.15(0.37,0.54,5.93)	+1.83	−3.7
Fe_B^{S-1}	+1.27(0.34,0.48,5.91)	+1.80	−3.7

The numbers in brackets for volume charge indicate s, p, d angular character. Reference Fe_2O_3 is chosen as anti-ferromagnetic corundum, FeO as paramagnetic rocksalt, V_2O_3 as non-magnetic conrundum, VO as non-magnetic rocksalt, V_2O_5 as non-magnetic orthorhombic.

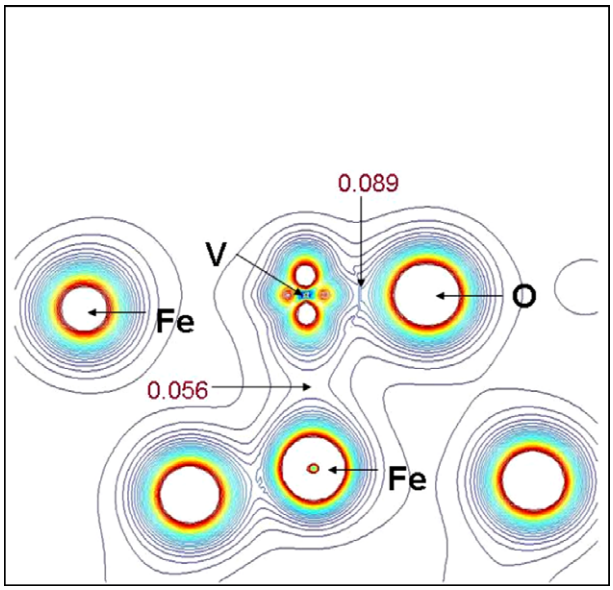

Fig. 3. Total charge density (equal interval) contour map for 0.5 ML V_B/Fe–hematite. The plane is perpendicular to (010) direction, including singly adsorbed V_B, Fe_B^{S-1} and one of the three surface O atoms. V–O and V–Fe bond critical point densities are indicated (e/a_0^3 $a_0 = 1$ Bohr).

Table 5
Analytic Mulliken charge, volume integrated charge, and bond orders derived from embedded-cluster calculations

	Mulliken charge (e)	Volume charge (e)	Bond order (e)
Clean Fe–hematite			
Fe_A^S	+2.31	+2.01	
Fe_B^{S-1}	+2.51	+2.12	
Fe_C^{S-1}	+2.55	+2.21	
0.5 ML V_B/Fe–hematite			
V_B	+1.91	+1.43	V_B–Fe_A^S 0.03
Fe_A^S	+2.21	+1.90	V_B–O^S 0.12
Fe_B^{S-1}	+1.82	+1.71	V_B–Fe_B^{S-1} 0.39
Fe_C^{S-1}	+2.54	+2.16	
Clean O_3–hematite			
Fe_B^{S-1}	+2.52	+2.13	
Fe_C^{S-1}	+2.47	+2.12	
0.5 ML V_A/O_3–hematite			
V_A	+2.55	+1.90	V_A–O^S 0.07
Fe_B^{S-1}	+2.47	+1.65	
Fe_C^{S-1}	+2.47	+1.65	

other configurations show a similar magnitude. This shift reflects the fact that deposited V can compensate excess negative charge at the O_3–hematite surface, by donating electrons to subsurface Fe and to the diffuse O 2p valence band. V_C is by far the least favored site; a prediction we shall return to later.

Table 3b gives a summary of adsorption geometry for 0.5 ML V/O_3–hematite. The distance between O^S and Fe^{S-1} ions is enlarged and the interlayer distances are increased, very similar to the V/Fe–hematite case discussed previously. The V–O bond length is shorter than that for the Fe-terminated case (1.73 Å vs. 1.79 Å), implying a stronger bonding tendency for V on O_3–hematite surface. The short $V_C^-Fe^{S-1}$ distance of 2.13 Å suggests a strong metal–metal interaction, which if repulsive would correlate with the lower site binding energy.

Table 6
Core level shift ΔE (eV) for 0.5 ML V_B/Fe–hematite, 0.5 ML V_A/O_3–hematite, and corresponding O-coverage

V_B/Fe_A hematite	Clean	1/3 ML O	2/3 ML O	1 ML O
V_B	0.00	0.78	0.91	0.20
Fe_A^S	−0.68	−0.14	0.34	0.56
Fe_C^{S-1}	−0.27	−0.27	−0.12	0.02
Fe_B^{S-1}	−0.27	−0.34	0.10	0.09
Fe_A^{S-2}	0.25	0.38	0.34	0.19

V_A/O_3-hematite	Clean	1/3 ML O
V_A	0.22	−0.19
Fe_C^{S-1}	−0.10	0.12
Fe_B^{S-1}	0.03	0.07
Fe_A^{S-2}	0.07	−0.17

The reference value for Fe is the same site before V adsorption, the reference state for V is V^{3+} in V_2O_3. The calculation is done within the initial state approximation.

3.2.2. Electronic and bonding properties

Fig. 4 gives site resolved DOS for a pure O_3-terminated surface, and for 0.5 ML V_A/O_3–hematite. For the ideal O_3-terminated surface, there is a broad hybridization between O^S 2p and Fe^{S-1} 3d electrons, as expected. After V adsorption, such hybridization splits into high binding energy bands with O 2p orbital domination and a low binding energy band with Fe 3d orbital domination and smaller O 2p contribution. The V atom DOS is divided into non-bonding and upper valence band regions, as in the Fe-terminated case.

Table 4c summarizes our results for electronic population analysis and magnetic moments. The Bader analysis suggests that there is only minor reduction for subsurface Fe after 0.5 ML V_A adsorption, by 0.15 e (Fe_C^{S-1}) and 0.13 e (Fe_B^{S-1}), corresponding to almost no change in oxidization state by comparison with the reference compound. The adsorbed V_A bears a Bader charge of +1.59 e, indicating a little bit higher than 2^+ oxidization state; the R_S volume integration gives about +1.11 e, roughly the same as in 0.5 ML V/Fe–hematite. In R_S volume integration, we see a smaller number of electrons after adsorption both total and in each orbital for subsurface Fe^{S-1}. This apparent oxidization, contradicting Bader analysis, is probably due to the fact that after V adsorption, the O–Fe bonding length is greatly enlarged, therefore, some electrons shared by O and Fe are actually moving out of the R_S sphere. For V_A, a local magnetic moment of 0.8 μ_B is predicted while the Fe^{S-1} moments dramatically increase from -1.7 μ_B to -3.6 μ_B, close to the value for the Fe-terminated hematite surface.

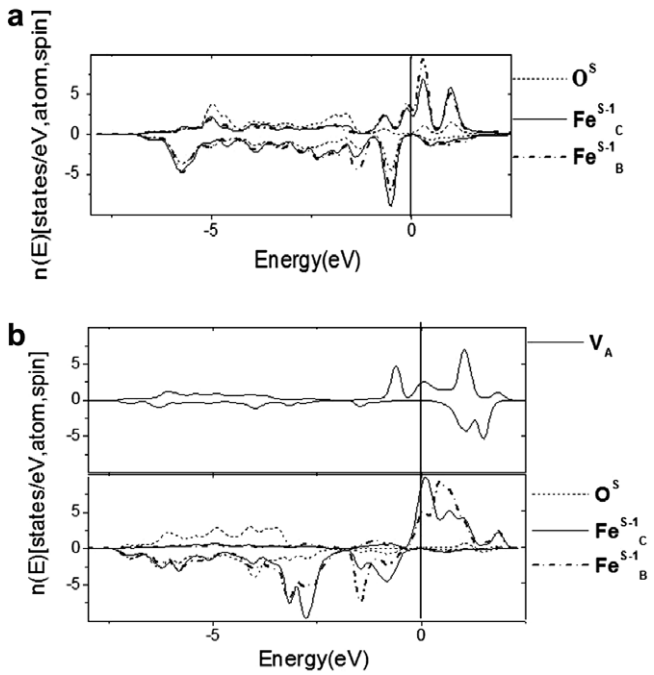

Fig. 4. Atom-resolved DOS for (a) O_3–hematite (0001), (b) 0.5 ML V_A/O_3–hematite.

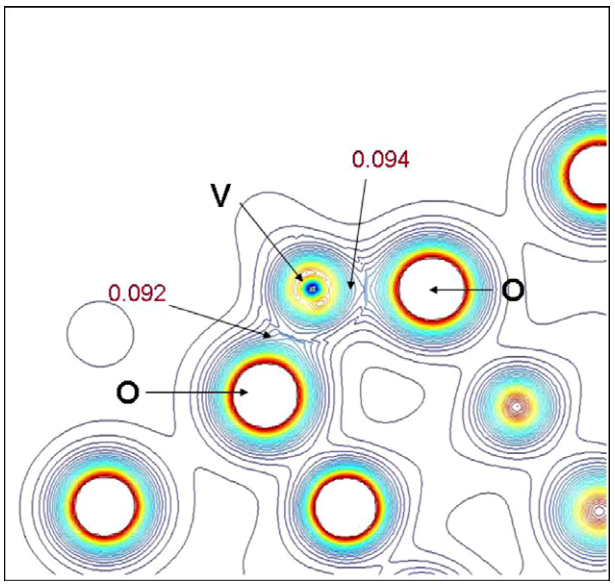

Fig. 5. Total charge density (equal interval) contour map for 0.5 ML V_B/O_3–hematite. The plane includes singly adsorbed V_A, and two of the three surface O atoms. V–O bond critical point densities (e/a_0^3) are indicated.

Table 5 gives the cluster analysis electronic population data for 0.5 ML V/O_3–hematite, showing 0.07 e bond order per V–O pair, or 0.21 e shared charge per site. Considering the charge density maps (see below) it is surprising that the bond charge is not larger. The oxidization of V is higher (2.55 e in Mulliken and 1.90 e in volume integration) compared with 0.5 ML V/Fe–hematite, due to the stronger V–O bonding. Mulliken charges for Fe B- and C-sites show no change compared to the clean surface, while volume charge shows a distinct reduction, to 1.65 e. The valence charge density of Fig. 5 is drawn for a single V atom on O_3/hematite, where we find the critical-point charge density to be 0.092 and 0.094 e/a_0^3 for both visible V–O bonds. This clearly shows the expected strong covalent character in V–O bonds, at the favored symmetrical O_3 hollow site.

3.2.3. Core level shift

In calculation of core level shifts (Table 6), we find that V core levels have a higher binding energy (in initial state approximation) by 0.22 eV than in the V^{3+} reference state; this is in conflict with the Bader analysis that suggests V_A has more electrons than V^{3+}. This again reflects the mixed ionic–covalent character of V–O bonding at the surface, and reminds us that core level shifts are not always directly correlated with net ionic charges. Supercell calculations on the V 2p core hole for V_nO_m overlayers on alumina suggest that the final state (valence only) screening effects may amount to ±0.2 eV for the top-most layers, and for V_2O_3(0001) up to 0.5 eV [22]. The subsurface Fe have small core level shifts, not more than 0.1 eV for A and B sites. Thus, the rather small Fe population and charge rearrangement is also reflected in a small potential change.

4. Results: atomic oxygen adsorption on submonolayer V/hematite

Here we study atomic oxygen adsorption on representative 0.5 ML V/hematite model surfaces. We assume that O adsorption will take on 1×1 supercell symmetry without any longer-ranged reconstruction or disorder, and that O only adsorbs on top of the surface instead of penetrating to subsurface sites. We expect that this simple model can bring insight about the resulting geometric and electronic properties changes upon O adsorption on V/hematite (0001) necessary for understanding the certainly more complicated actual oxidization process.

In modeling atomic O adsorption on a V/hematite surface, we study three types of coverage, 1/3 ML, 2/3 ML and 1 ML, following the notation of Czekaj et al. [35] where the atomic density of an ideal oxygen plane along (0001) is referred to as 1 ML. The pre-adsorbed V/hematite surfaces are chosen from the representative energy-favorable configurations obtained from our previous calculations: 0.5 ML V_B/Fe_A–hematite and 0.5 ML V_A/O_3–hematite. For configurations that have only one metal atom at the surface, we found that O will adsorb on top of the metal to form a M=O double bond (M = V, Fe). For configurations that have more than one surface metal atom, we found that O prefers binding at M–M′ bridge sites to form a M–O–M′ group. A previous study of O adsorption on the V_2O_3(0001) surface also concluded that for a multi-metal terminated surface such bridge site adsorption can give the most stable adsorbate–substrate complex [35].

4.1. O adsorption on 0.5 ML V/Fe–hematite

4.1.1. Adsorption sites, geometry and energy

Adsorption energy calculations for different O coverage on 0.5 ML V/Fe–hematite are summarized in Table 2. On this surface, at low coverage (1/3 ML), the favored site is bridging, almost directly above the V–Fe midpoint, with adsorption energy of 7.40 eV/atom. At intermediate coverage O (2/3 ML), bridging sites that are slightly displaced from the bulk O site are favored, with E_{ads} of 6.62 eV/atom. For 1 ML O adsorption, we find a stable configuration at the hematite bulk O site, with adsorption energy equal to 6.01 eV/atom. The reduced adsorption energy found for increasing O coverage can be attributed to the larger repulsion among adsorbate atoms. We notice that a simple thermodynamic calculation (Eq. (4)) suggests that 1 ML O coverage achieves lowest free energy. However, we have reason to doubt the reality of this result, since conventional DFT is notorious for its trend to overestimate binding energy: a typical example is for hematite (0001) surface termination, where the O_3-terminated surface is predicted to be stable under oxidized environment in conventional DFT but not so in GGA + U calculations [9].

Table 3c collects detailed structural information for the most stable adsorption configurations for various O coverage on 0.5 ML V–Fe–hematite, while Fig. 6a and b show the model for low and high coverage. The O_{ads}–V bond length depends very little on O coverage, all three cases yielding ~1.7 Å; however, the O–Fe bond length variance is a little bit larger; e.g., for 2/3 ML O adsorption, two O_{ads}–Fe bonds differ by as much as 0.1 Å (1.92 Å vs. 2.02 Å). The repulsion between adsorbed and surface O causes buckling among O atoms. This effect is largest for 1/3 ML coverage, smaller for 2/3 ML, and least for 1 ML O. With reference to the O^S plane average height, the adsorbed O is 2.02 Å higher for 1/3 ML, 2.19/2.26 Å for 2/3 ML and 2.09 Å for 1 ML. The substrate also experiences a large geometry change due to the adsorption of O: for instance, the V that is originally at the same height as O^S moves upward dramatically as O adsorbs, while the O^S–Fe^{S-1} distance becomes smaller. The height difference between two Fe_C^{S-1}–Fe_B^{S-1} atoms becomes smaller. The geometry effects induced by adsorbed O are localized within the surface region; below the O^{S-1} layer the structure changed very little.

4.1.2. Electronic and bonding properties

Fig. 7 gives DOS for 1/3 ML and 1 ML O on 0.5 ML V_B/Fe–hematite. It can be seen that the adsorbed O_b has a lower binding energy 2p orbital than that of the hematite

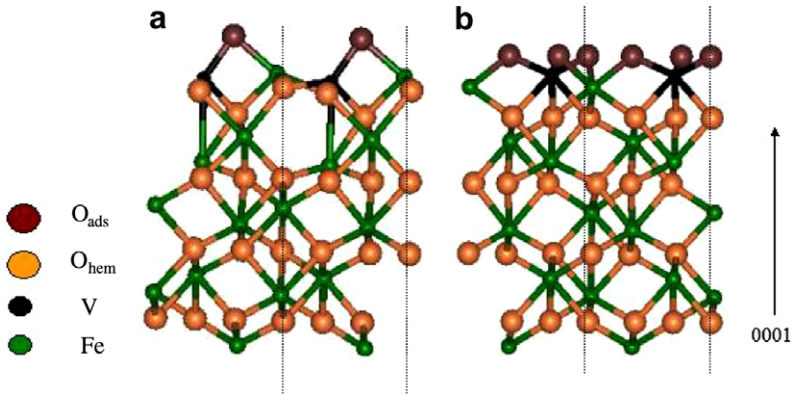

Fig. 6. Models for O adsorption on V/Fe–hematite. (a) 1/3 ML O on 0.5 ML V_A and (b) 1 ML O on 0.5 ML V_A.

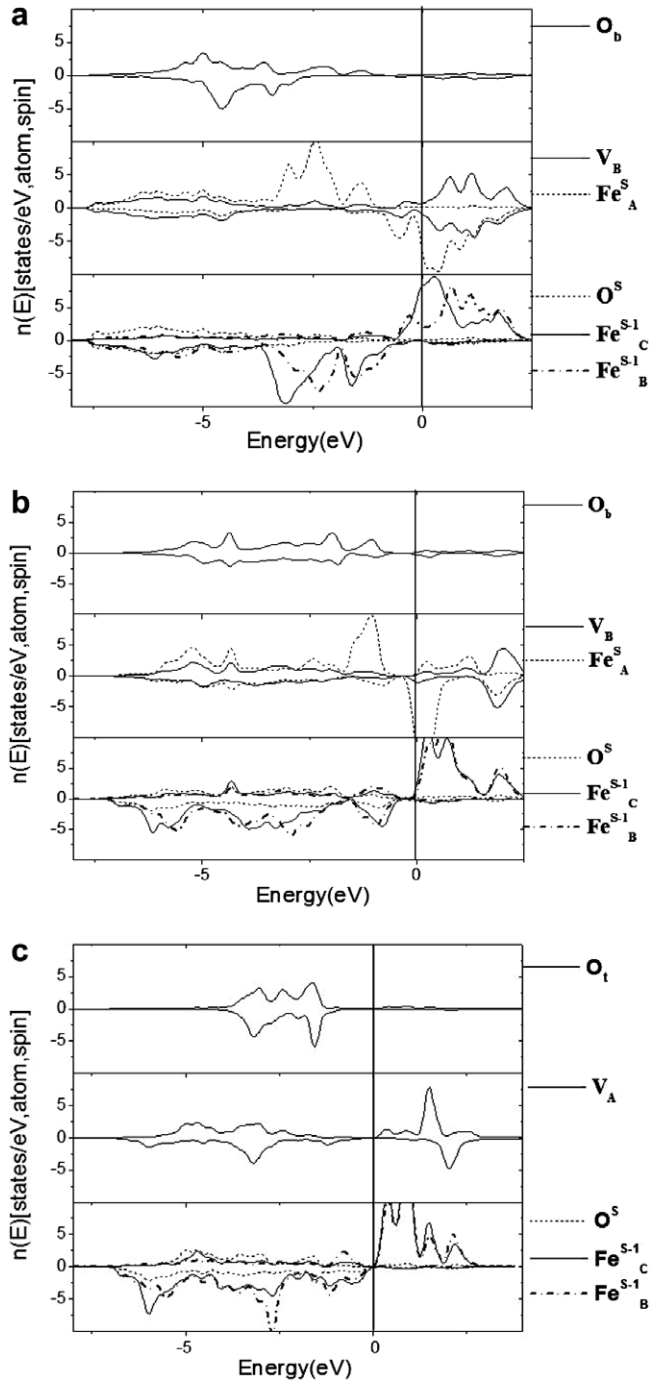

Fig. 7. Atom-resolved DOS for oxygen adsorbed on 0.5 ML V_B/Fe–hematite: (a) 1/3 ML O, (b) 1 ML O, and on 0.5 ML V_A/O_3–hematite: (c) 1/3 ML O.

surface O^S orbitals, due to the lower coordination number of the adsorbate. As coverage increases, the O_b 2p DOS becomes broader, indicating its increased self-interaction and interaction with neighboring atoms. For all coverages, both O_b 2p and O^S 2p orbitals show strong hybridization with V and Fe^S_A 3d electrons. Comparing low and high coverage O adsorption, there is a clear shift towards higher energy (closer to E_f) of V_B and Fe^S_A DOS for 1 ML relative to 1/3 ML. This reflects the trends of stronger interaction between (V, Fe) and O_b and weaker interaction between (V, Fe) and O^S.

Table 4 summarizes the electronic configurations found for O −0.5 ML V_B/Fe–hematite in VASP calculations. In Bader analysis, we see that after 1/3 ML O adsorption, both Fe^S_A and Fe^{S-1}_B are partially reoxidized, from +1.22 e and +1.29 e, respectively, to +1.45 e and +1.48 e. There is a minor increase in electron population for Fe^{S-1}_C, net charge changing from 1.64 e to 1.60 e. As O coverage increases, all three Fe continue losing electrons, and at 1 ML coverage, the atomic charge is similar to that in Fe_2O_3, indicating that Fe are fully reoxidized to the 3+ state. V is also further oxidized as O coverage increases from 1.62 e at no coverage, then 1.99 e at 1/3 ML, 2.12 e at 2/3 ML and finally 2.20 e for 1 ML. At 1 ML, V is essentially in its 5+ state; i.e., far beyond the value of 1.86 e for the reference compound V_2O_3. From R_S volume charge integration, we deduce that O adsorption induces a considerable spatial shape change and occupation change of 3d electron orbitals around Fe^S_A, V_B and Fe^{S-1}_C: this can be seen by looking at the irregular variation of volume charges versus coverage for these sites. For Fe^{S-1}_B, the R_S trend is much more consistent with the Bader analysis, implying a relatively stable orbital spatial distribution. It can be seen from the Table that the d orbital depopulation contributes mostly to reoxidization of Fe; however, significant rehybridization occurs among Fe s, p, and d orbitals. With 1/3 ML and 2/3 ML O, the magnetic moment of Fe^S_A is practically restored to the value before V deposition (3.4 μ_B, see Table 1), while the deposited V lose almost all magnetic moment, a sign of complete oxidization. The significant V d-electron occupancy reflects participation in V–O covalent bonding, and not in V-localized magnetic orbitals. As O coverage increases to 1 ML, however, the Fe^S_A magnetic moment falls again, to only 1.4 μ_B, similar to that of the Fe^{S-1} atom in O_3-hematite. Thus the surface-region Fe moment is a very sensitive indicator of the local chemical environment.

4.1.3. Core level shift

The V core level shifts of +0.20 to +0.91 eV (initial state approximation) for varying levels of oxygen coverage (Table 6) provide evidence that for each of the optimized local sites, the metal is further oxidized, in agreement with charge and DOS analyses. There is a significant variation of the V core potential, depending upon site and coverage which might be exploited in high resolution measurements. The gradual "recovery" of Fe^S, Fe^{S-1}, and Fe^{S-2} oxidation states with increasing oxygen coverage is also evident.

In order to evaluate the importance of final state screening effects, we further considered 38- and 50-atom molecular clusters centered on V_B, allowing for both core and valence electron relaxation in an optimized numerical LCAO basis. Ground state, Slater transition state (TS), and the full core hole state were calculated for comparison of energy levels and charge distributions. The large quantitative importance of charge transfer from neighbors and

the resulting screening is immediately apparent; e.g., the total energy difference (LDA, non-relativistic) for the isolated V^{3+} $2p^6 \Rightarrow V^{4+}$ $2p^5$ ionizing transition is 620.7 eV, while the experimental $2p_{3/2}$ XPS band appears at ~515.3 eV. The cluster transition state calculations give an ionization band of width ~2.5 eV (due to exchange coupling of the core hole to the valence states) centered at ~509.4 eV. More accurate results would presumably require a relativistic treatment of the $2p_{3/2}$, $2p_{1/2}$ sub-bands. The diagnostic of greatest interest at present is the level shift between V_B//Fe_A and O/V_B/Fe_A (1/3 ML O) environments, for which we find TS predictions of 0.52–0.85 eV for the two possible core spin orientations. This brackets the initial state estimate of 0.78 eV given in Table 6, suggesting that while final state screening is not of over-riding importance, it can contribute several tenths eV to the observed values. The width of the experimental bands due to core hole lifetime and instrumental broadening limits the precision of theory-experiment comparisons, but it might be possible to gain more information by controlling the polarization of the input X-rays and/or selecting on spin of the photoelectrons.

4.2. O adsorption on 0.5 ML V/O_3–hematite

4.2.1. Adsorption sites, geometry and energy

The data for adsorption energy and sites for O adsorption on 0.5 ML V/O_3–hematite are collected also in Table 2. We find that only 1/3 ML O can be stably adsorbed onto this surface, where a vanadyl bond V=O is formed (see Fig. 8) with net binding energy 6.56 eV. Originally three-coordinated with surface O atoms, V now adopts a slightly distorted tetrahedral coordination, similar to that suggested in Ref. [11]. The bond length between V_A and the adsorbed O is 1.61 Å (Table 3), a typical V=O value found in previous studies of $V_2O_5(0\,1\,0)$ and $V_2O_3(0\,0\,0\,1)$ surfaces [33,35]. Compared to the pre-adsorption V/O_3–hematite system (Table 3), we can see here that the on-top O leads to significant changes in near-surface bond lengths and interlayer relaxations. The average V–O bond length increases from 1.73 Å to 1.81 Å, while the Fe^{S-1}–O^S bonds of the sub surface layer decrease from 2.03/2.19 Å to 1.93/2.12 Å, suggesting a partial reoxidization of Fe. These bond length changes lead to only one notable modification for interlayer relaxation: V_A shifts up by 0.25 Å relative to the O^S plane.

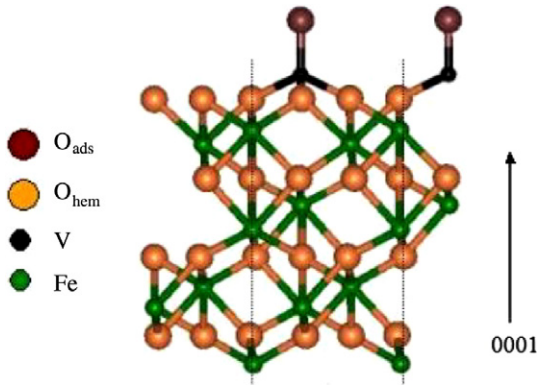

Fig. 8. Models for O adsorption on V/O_3–hematite: 1/3 ML O on 0.5 ML V hematite.

4.2.2. Electronic and bonding properties

Fig. 7 gives the DOS for 1/3 ML O adsorption on the 0.5 ML V_A/O_3–hematite surface. Similar to electronic structure analysis given in previous sections, we can see that O_{ads} has an apparent higher-lying energy band than hematite surface O. The hybridization between O^S and V, Fe_C^{S-1}, Fe_B^{S-1} is strong and extensive; for Fe, this is a clear sign of its reoxidization; for V, it can be seen that its non-bonding conduction band shifts to lie well above E_f, indicating a 5+ full oxidization state. Table 4 summarizes the electronic configurations and charges for O–0.5 ML V_A/O_3–hematite. For 0.5 ML O, with the Bader charge of +2.19 e for V_A indicating reoxidization to the 5+ state, the subsurface Fe are also reoxidized to the 3+ state with net charge of 1.83 e for Fe_C^{S-1} and 1.80 e for Fe_B^{S-1}. In the R_S volume charge integration, the V_A charge of +1.00 e is pretty close to the value of 1.11 e before O adsorption (Table 4), implying that most localized electrons that form bonds with O are still within R_S, so that the Bader analysis indicates transfer from the outer valence region. The volume charges for Fe_C^{S-1} and Fe_B^{S-1} (1.15, 1.27 e) are almost unchanged compared to pre-O adsorption (1.16, 1.21 e). The adsorbed V has a net magnetic moment of $-0.2\ \mu_B$, while the subsurface Fe's magnetic moments are restored to bulk value of $-3.7\ \mu_B$. In Table 6 we see the additional (initial state) core level shift of 0.4 eV upon formation of the V=O bond; note however, that the shift is in the opposite direction to that expected for a simple charge transfer, due to the simultaneous lattice relaxation and charge redistribution. The Fe^{S-1} and Fe^{S-2} sites report opposite shifts to each other, again indicating a more subtle rebalancing of surface region potentials, beyond that implied by simple Fe re-oxidation seen in charge analysis.

5. Comparison of experiment with theory

We now compare our calculated results with the work of Kim et al. [11], where the adsorption geometry and electronic structure for 0.5 ML V adsorption on a hematite (0001) surface were inferred from surface X-ray standing wave and XPS measurements. With respect to the most favorable adsorption sites for 0.5 ML V deposited on a clean hematite surface, Kim and coworkers reached a conclusion that about 50% of the adsorbed V atoms are ordered, the rest being in a disordered state not visible in diffraction. Among the ordered adsorbed V atoms, approximately half of them (occupancy 0.33) adopt the threefold hollow site A with height of ~0.6 Å relative to a bulk oxygen plane, and the other half (occupancy 0.27) adopt site C with height approximately 1 Å higher than V_A. Upon oxidization, changes in the (0006), $(10\bar{1}4)$, and $(01\bar{1}2)$ XSW

phase and amplitude were interpreted as exchange of vanadium at site C for site B. Some atoms are 'lost' to the disordered phase, with a best fit to (V_A, V_B, V_C) occupancy being (0.33, 0.08, 0.0). XPS data showed an as-deposited V $2p_{3/2}$ binding energy of 515.3 eV, about 0.5 eV less than reference values for V^{3+}, and a value of 516.9 eV, about 0.3 eV less than V^{5+} reference values, for the oxidized state. XPS data for Fe 2p also showed partial reduction of Fe upon V deposition, and re-oxidation upon exposure to atomic oxygen.

Our calculations predict that for an ideal single-Fe-terminated hematite, site B will be most preferred for 0.5 ML V deposition; and for ideal O_3-terminated surfaces, site A. No matter what surface termination is considered, site C is energetically unfavorable, largely due to repulsion from the nearby subsurface Fe atom. The energy difference between the preferred adsorption configurations and site C is well above any reasonable error estimates concerning density functional theory or computational precision. We found that predicted Fe oxidation state change and core level shifts for V deposition on hematite and subsequent oxidation are consistent with experiment, noting that the sub-surface Fe in O_3-terminated hematite are already rather well 'protected' against change. However, all our calculations predict that V is only mildly oxidized upon deposition; for example, the Bader charges of 1.62 and 1.59 e for 0.5 ML V on Fe- and O_3-terminated hematite, respectively, are intermediate to those of V^{2+} and V^{3+} reference compounds. This is understandable in terms of the lower surface coordination to ligands, and reminds us again that electronic core binding energies are not a simple measure of oxidation state. The strong charge transfer calculated for O/V/hematite oxidation environments is in accord with chemical intuition and in agreement with experimental interpretations.

As to the causes of the obvious discrepancy between experimental interpretation of site occupancy and the models presented here, one immediately wonders if the 1×1 surface meshes treated are too simple/limited to describe some particular surface reconstruction which may be dominant. The major problem of experimental interpretation is that XSW measurements only reveal orientations and heights relative to *subsurface bulk* structure, while giving no information on the arrangements of relaxed, possibly defective and non-stoichiometric surface-region hematite layers. The XSW-derived models do certainly suggest that some surface regions are more complex. In a simple test, in which the subsurface Fe below site C was removed, the binding energy of V_C increased to become very similar to that of the sites A and B, confirming our hypothesis about the V–Fe repulsion. However, for lack of any further structural or chemical data, we chose not to pursue the implied non-stoichiometric surface models further. As a final test, we briefly considered a 2×2 surface cell, with one Fe_A vacancy per cell and found no tendency toward large-scale reconstruction. We next discuss other possible causes of error or misinterpretation.

We consider that the general theoretical methodology used, and the DFT approach in particular, are adequate to describe the binding properties of the metal–oxide interface, in view of many successful applications to oxide surfaces. The underlying electrostatic interactions are probably dominant, although we do not entirely discount the inadequate description of 3d–3d electronic correlation effects. Our GGA + U model calculations do suggest that this is not a critical factor for adsorption sites/energies. Final state effects not included in our core level shift analysis could skew the results, both for core level energy shifts and charge state analysis. Molecular cluster calculations on the V_B/Fe_A and $O/V_B/Fe_A$ interfaces suggest that final state screening could amount to a few tenths eV, but is not dominant. We also recall that Bader analysis, indeed any charge partitioning scheme (of which we have demonstrated several), gives only a qualitative or relative measure of the chemical state of atoms. Finally, an "ionic charge" defined by whatever means is not necessarily closely correlated with XPS binding energy change, which depends upon both long- and short-range potentials.

The working surface is achieved by annealing of a single crystal, which implies the presence of surface defects and impurities as well as multiple domains of possibly different (Fe and O) terminations. Significantly, the work function drop is measured as ~1.6 eV, about half-way between the calculated work function drop for either pure Fe-terminated surface (~0.1 to 0.2 eV) or O_3-terminated surface (3–4 eV). Fabrication of hematite surfaces by other methods may also yield a mixed termination surface [7,10]. Therefore, it is very likely that in the experiments reported by Kim et al., some part of the surface is single Fe-terminated and some part of the surface is locally like O_3-termination, while the whole surface still maintains corundum structure. This can be consistent with the LEED measurement that observes a sharp (1×1) hematite pattern and our calculation (not reported here) that suggests that introducing an Fe vacancy every (2×2) unit cell causes little reconstruction of the surface.

Therefore, in order to rationalize theory vs. experiment, we suggest that when V is deposited the visible (ordered) portion tends to concentrate on the O_3-terminated region. This conjecture is supported by our calculation that average adsorption energy for 1 ML V depositing on an O_3–hematite surface (discussed in detail in the following article) is larger than even the highest adsorption energy for 0.5 ML V on a Fe-terminated surface. Therefore, the O_3-terminated area tends to have two V deposited per unit cell. Under these conditions, we may posit that the two V depositing onto O_3-terminated areas actually do occupy sites A and C, as proposed experimentally. In fact, our calculated geometry for 1 ML (V_C, V_A) configuration is very close to what is inferred in XSW measurements; for example, V_C is 1 Å higher than V_A. Also it is found that the (V_C, V_A) configuration induces very little change in substrate structure while (V_A, V_B) and (V_B, V_C) structures need relatively large surface relaxation which might induce large structure mismatch between O_3-terminated regions and Fe-terminated regions. Thus the energy gain for V depositing

on (V_A, V_B) could be well offset by such domain structure mismatch; e.g., kinetic factors prevent reaching the thermodynamically favored state. It is worth recalling that both deposition and oxidation occur with substrate at room temperature where diffusion is restricted.

6. Summary and conclusions

In this work we investigated geometric and electronic properties of two systems:

(1) Half monolayer V adsorption on a hematite (0001) surface with two idealized bulk cut terminations; and (2) atomic O adsorption on the V/Hematite system. In the first models, we calculated the energy and relaxed structure of V adsorbed onto a hematite (0001) surface, studying its electronic structure using both plane wave projected density of states and cluster analysis. We found that threefold bonding of V with a hematite surface O, at a position where no Fe is directly below, is the most stable configuration. In the second set of models, we studied atomic O adsorption on the V/Hematite system under different coverages, finding that O forms strong bonds with surface Fe or V, causing them to be oxidized. A detailed picture of both V and surface-region Fe oxidation and reduction processes was obtained, using several complementary charge analysis models and core level shift data. Adsorption of O also was predicted to induce large surface structural changes.

By comparing our results with experimental XSW and XPS interpretations, we find agreement with the "chemically obvious" metal V_A site, but apparent disagreement between theoretical prediction and experiment measurement with respect to submonolayer V adsorption on the V_C site. We conjecture that imperfect surfaces, preferential ordering onto O_3-terminated domains, and possible complex surface-region hematite reconstruction and kinetic factors might help reconcile theory vs. experiment. Since very little is currently known about the surface morphology and composition, we cannot conclusively identify the cause for theory-experiment discrepancies. Further research is needed, particularly to discover the disposition of the "amorphous" half of deposited V, and the geometry of reconstructed surface-region hematite layers.

Acknowledgements

This research was supported by the Chemical Sciences, Geosciences and Biosciences Division, Office of Basic Energy Sciences, Office of Science, US Department of Energy, Grant No. DE-FG02-03ER15457. The work of J.J. Jin was supported by the MRSEC Program of the National Science Foundation (DMR-0076097) through the Materials Research Center of Northwestern University.

References

[1] V.E. Henrich, P.A. Cox, The Surface of Metal Oxides, University Press, Cambridge, 1994.
[2] G.C. Bond, S.F. Tahir, Appl. Catal. 71 (1991) 1.
[3] I.E. Wachs, Catal. Today 27 (1996) 437.
[4] S. Surnev, M.G. Ramsey, F.P. Netzer, Prog. Surf. Sci. 73 (2003) 117, and references therein.
[5] J. Biener, M. Bäumer, J. Wang, R.J. Madix, Surf. Sci. 450 (2000) 12.
[6] J. Biener, M. Bäumer, R.J. Madix, P. Liu, E. Nelson, T. Kendelewisz, G. Brown Jr., Surf. Sci. 449 (2000) 50.
[7] X.G. Wang, W. Weiss, S.K. Shaikhutdinov, M. Ritter, M. Petersen, F. Wagner, R. Schlögl, M. Scheffler, Phys. Rev. Lett. 81 (1998) 1038.
[8] W. Bergermayer, H. Schweiger, E. Wimmer, Phys. Rev. B 69 (2004) 195409.
[9] A. Rohrbach, J. Hafner, G. Kresse, Phys. Rev. B 70 (2004) 125426.
[10] M.E. Greene, A.N. Chiaramonti, S.T. Christensen, L.X. Cao, M.J. Bedzyk, M.C. Hersam, Adv. Mater. 17 (2005) 1765.
[11] (a) C.-Y. Kim, A.A. Escuadro, P.C. Stair, M.J. Bedzyk, J. Phys. Chem. C 111 (2007) 1874;
(b) C.-Y. Kim, M.J. Bedzyk, Thin Solid Films 515 (2006) 2015.
[12] S.L. Dudarev, A.I. Liechtenstein, M.R. Castell, A.D. Briggs, A.P. Sutton, Phys. Rev. B 56 (1997) 4900;
S.L. Dudarev, G.A. Botton, S.Y. Savrasov, C.J. Humphreys, A.P. Sutton, Phys. Rev. B 57 (1998) 1505.
[13] O. Bengone, M. Alouani, P. Blochl, J. Hugel, Phys. Rev. B 62 (2000) 16392.
[14] A. Rohrbach, J. Hafner, G. Kresse, J. Phys.: Condens. Mat. 15 (2003) 979.
[15] G. Kresse, J. Hafner, Phys. Rev. B 49 (1994) 14251.
[16] G. Kresse, J. Hafner, Phys. Rev. B 47 (1993) 558.
[17] G. Kresse, J. Furthmuller, Comp. Mater. Sci. 6 (1996) 15.
[18] G. Kresse, J. Furthmuller, Phys. Rev. B 54 (1996) 11169.
[19] P.E. Blöchl, Phys. Rev. B 50 (1994) 17953;
G. Kresse, J. Joubert, Phys. Rev. B 59 (1999) 1758.
[20] J.P. Perdew, K. Burke, M. Ernzerhof, Phys. Rev. Lett. 77 (1996) 3865.
[21] H. Monkhorst, J.D. Pack, Phys. Rev. B 13 (1976) 5188.
[22] T.K. Todorova, M.V. Ganduglia-Pirovano, J. Sauer, J. Phys. Chem. B 109 (2005) 23523.
[23] (a) G. Henkelman, A. Anraldsson, H. Jonsson, Comp. Mater. Sci. 36 (2006) 254;
(b) G. Henkelman, A. Arnaldsson, H. Jonsson, Bader Charge Analysis Program, <http://theory.cm.utexas.edu/bader/>.
[24] (a) M. Methfessel, Vincenzo Fiorentini, Sabrina Oppo, Phys. Rev. B 61 (2000) 5229;
(b) VASP manual is available at <http://cms.mpi.univie.ac.at/vasp/vasp/vasp.htm>.
[25] E.J. Baerends, D.E. Ellis, P. Ros, Chem. Phys. 2 (1973) 41.
[26] B. Delley, D.E. Ellis, J. Chem. Phys. 76 (1982) 1949.
[27] S.H. Vosko, L. Wilk, Phys. Rev. B 22 (1980) 3812.
[28] D.E. Ellis, G.A. Benesh, E. Byrom, Phys. Rev. B 20 (1979) 1198.
[29] M.P. Tosi, Solid State Physics, Academic, New York, 1964.
[30] R.F.W. Bader, Atoms in Molecules – A Quantum Theory, Oxford University Press, 1990.
[31] X. Ma, Ph.D thesis, Northwestern University, 2007.
[32] X. Ma, Li Liu, J. Jin, P.C. Stair, Don. E. Ellis, Surf. Sci. 600 (2006) 2874.
[33] E.R. Batista, R.A. Friesner, J. Phys. Chem. B 106 (8136) (2002).
[34] G. Kresse, S. Surnev, J. Shoiswohl, F.P. Netzer, Surf. Sci. 555 (2004) 118.
[35] I. Czekaj, K. Hermann, M. Witko, Surf. Sci. 545 (2003) 85.